Chapter 2

Micromechanics of Elastic Metamaterials

Xiaoming Zhou,[a] Xiaoning Liu,[a] Gengkai Hu,[a] and Guoliang Huang[b]

[a]*School of Aerospace Engineering, Beijing Institute of Technology, Beijing 100081, China*

[b]*Department of Systems Engineering, University of Arkansas at Little Rock, Little Rock, Arkansas 72204, USA*

zhxming@bit.edu.cn, liuxn@bit.edu.cn, hugeng@bit.edu.cn, glhuang@ualr.edu

This chapter presents the basic principles of design, characterization, and applications of elastic metamaterials. Metamaterials are artificial materials engineered to have properties that may not be found in nature. Elastic metamaterials gain unusual properties from their subwavelength microstructures, through local resonances to create negative values of effective mass, effective bulk or shear modulus. Although the content is not able to include all the advances in such interdisciplinary field, it provides readers a comprehensive overview on wave characteristics of elastic metamaterials.

2.1 Introduction

Responses of matters to elastic waves are characterized by effective mass and modulus, provided that the wavelength of perturbations

Handbook of Micromechanics and Nanomechanics
Edited by Shaofan Li and Xin-Lin Gao

ISBN 978-981-4411-23-3 (Hardcover), 978-981-4411-24-0 (eBook)
www.panstanford.com

is sufficiently larger than the typical size of microstructures in the matter. By careful design of geometry and mechanical properties of microstructures, a class of materials with negative effective mass or modulus or anisotropic effective mass can be fabricated. These materials, usually termed metamaterials, offer an unprecedented way to manipulate wave propagation, such as acoustic cloaking and super resolution imaging. A material with simultaneous negative mass and modulus would have a negative refractive index, due to anti-parallel nature of phase and group velocities. The double-negative material is also called left-handed material, first imagined by Veselago [1] about 40 years ago for electromagnetic (EM) waves. It was not until the beginning of this century that Pendry [2, 3] and Smith [4, 5] made great contributions toward the realization of EM metamaterials, bringing the imagination into reality. Since then, metamaterials have gradually emerged as a new interdisciplinary field [6] attracting active researchers all around the world.

Lamb [7] proposed the concept of negative group velocity in a mechanical system in 1904. A suspended chain system is conceived to possess such property [8]. In 2000, Liu *et al.* [9] proposed the first acoustic metamaterial, which consisted of lead particles coated with soft rubber layers embedded in an epoxy matrix. A stopband for acoustic wave appeared, which has been attributed to the negative effective mass of the composite material. Later Fang *et al.* [10] proposed the use of Helmholtz resonators to generate negative effective modulus. The negative index material has also been designed with two populations of coated inclusions [11], so that negative mass and modulus dominated by dipolar and monopole resonances are engineered to be present at the overlapped frequencies. Liu *et al.* [12] proposed a compact design of negative index materials for elastic waves by use of the chirality of the microstructure, in which the rotational resonance of the particles induces a negative effective bulk modulus, while translational resonance is used to realize negative effective mass. Negative effective shear modulus is related with quadruple resonances [13]. A planar metamaterial with negative effective shear modulus has been conceived by the enhancement of the quadruple resonance [14]. Due to the resonant

effect, negative effective material parameters are often available in a limited bandwidth. To broaden the frequency range, Lee *et al.* [15] found that a membrane with a fixed boundary can be considered a metamaterial with negative effective mass below a cut-off frequency. A continuum material model was further developed by Yao *et al.* [16], which is very promising for low-frequency noise isolation. In order to clearly illustrate the mechanism of local resonance and its effect on the macroscopic property, mass–spring systems are usually used as model systems [17, 18]; for example, the dipolar resonance of a coated inclusion can be well represented by a mass-in-mass system. Much work has been devoted to examine the transmission property of mass–spring systems in the presence of local resonances [19, 20] and to study the active control of the resonances [21, 22].

Metamaterials greatly enlarge the space for material selection, so they can be patterned in the space to control acoustic and elastic waves. The relation between the functionality of a device and the material pattern in the space can be established by the transformation method [23, 24]. Due to the form invariance of Helmholtz's equation for acoustic waves, the geometry and material distribution are equivalent. It has been proved that the space transformation can be manipulated to define a device with targeted functionality, e.g., acoustic cloaking [25, 26]. For elastic waves, Navier's equation does not retain the form invariance [27]; so the exact controlling for elastic waves is not available yet. However under some constraint conditions, the elastic wave can still be controlled by patterning the microstructure of composites [28, 29].

In this chapter, mass–spring systems are first examined to clearly illustrate the mechanism of negative effective mass and modulus, and then their interplay with macroscopic property is discussed. The continuum versions of the corresponding mass–spring systems are explained in the second section, and their effective material properties will be derived based on dynamic homogenization techniques. The applications of elastic metamateials to cloaking and superlensing are discussed in the last section.

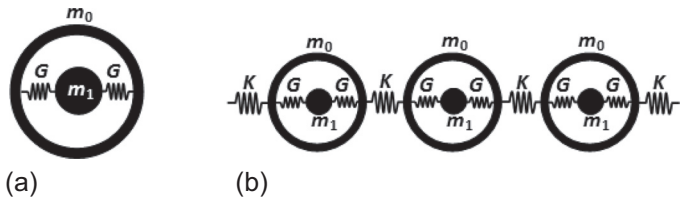

Figure 2.1 (a) The mass–spring structure with negative effective mass; (b) a one-dimensional lattice system composed of the mass–spring structure.

2.2 Discrete Mass–Spring Model of Metamaterials

2.2.1 *Negative Effective Mass*

Consider a mass–spring structure shown in Fig. 2.1(a), where an outer mass of weight m_0 is connected to an inner mass of weight m_1 by two massless springs of equal spring constant G. In the time harmonic case, let x_1 and x_0 denote, respectively, the complex amplitudes of displacements of the inner and outer mass. From the equilibrium equation of the inner mass, the following is obtained [18]:

$$\frac{x_1}{x_0} = \frac{\omega_1^2}{\omega_1^2 - \omega^2} \tag{2.1}$$

where $\omega_1 = \sqrt{2G/m_1}$ is the resonant frequency. When the force of complex amplitude F is acting on the outer mass, the equilibrium equation of the outer mass is written as

$$F + 2G(x_1 - x_0) = -m_0\omega^2 x_0 \tag{2.2}$$

Substitute (2.1) into (2.2) to obtain

$$F = -\left(m_0 - \frac{m_1\omega_1^2}{\omega^2 - \omega_1^2}\right)\omega^2 x_0 \tag{2.3}$$

The inner mass is hidden inside the outer mass; then it is possible to assign an effective dynamic mass m_{eff} to the seemingly solid mass. The definition of effective dynamic mass can be given under the assumption that the equivalent solid mass follows the same dynamic equation as Eq. (2.3). This means

$$F = -m_{\text{eff}}\omega^2 x_0 \tag{2.4}$$

where m_{eff} is given by

$$m_{\text{eff}} = m_0 - \frac{m_1\omega_1^2}{\omega^2 - \omega_1^2} \tag{2.5}$$

Equation (2.5) shows that m_{eff} will become negative at frequencies ranging from ω_1 to $\omega_1\sqrt{(m_1 + m_0)/m_0}$. As seen in Eq. (2.1), the inner mass moves in out-of-phase with respect to the out mass beyond the resonant frequency ω_1. The negative value of m_{eff} is due to the negative momentum of the inner mass with the amplitude larger than that of the outer mass with the positive velocity. When the inner mass is fixed, effective dynamic mass in Eq. (2.5) becomes

$$m_{\text{eff}} = m_0\left(1 - \frac{\omega_0^2}{\omega^2}\right) \tag{2.6}$$

In such case, m_{eff} is negative below a cut-off frequency $\omega_0 = \sqrt{2G/m_0}$. The corresponding continuum material model will be described below. Usually, the "dynamic" term in the effective dynamic mass is omitted. However, it should be understood that the effective mass of metamaterials is a dynamic parameter, characterizing the inertia effect and is very distinct from the static gravitational mass.

Wave characteristics of metamaterials with negative effective mass can be envisioned in a lattice system composed of the mass–spring structures connected with the springs of the spring constant K, as shown in Fig. 2.1(b). By imposing the Bloch's periodic condition, the dispersion relation for an infinite lattice system with the lattice distance L is derived to be

$$m_{\text{eff}}\omega^2 = 4K\sin^2\frac{qL}{2} \tag{2.7}$$

where q is the Bloch wave vector. At frequencies of $m_{\text{eff}} < 0$, it is found in Eq. (2.7) that the wave vector q takes purely imaginary values and the waves are forbidden in this frequency band.

In a finite-period lattice system shown in Fig. 2.2(a), the transmission properties of disturbances across the system can be evaluated to verify the blocking effects at frequencies of negative effective mass. The transmission coefficient $T = |X_N/X_0|$ is derived as [19]

$$T = \left|\prod_{n=1}^{N} T_n\right| \tag{2.8}$$

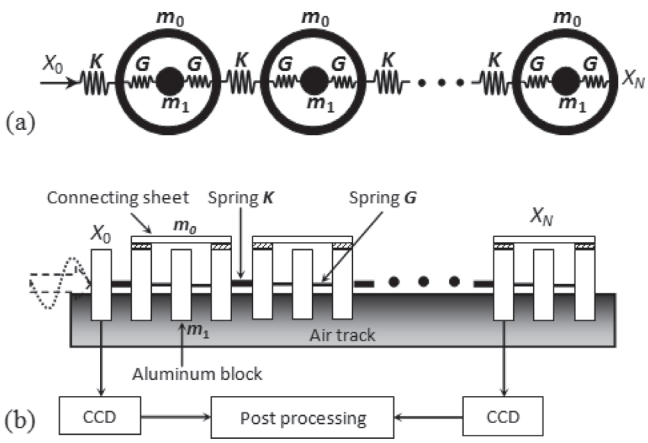

Figure 2.2 (a) Finite-period lattice system; (b) the scheme of the experimental setup.

with

$$T_n = \frac{K}{K(2 - T_{n+1}) - m_{\text{eff}}\omega^2}; n = 1, 2, \ldots, N \tag{2.9}$$

and $T_{N+1} = 1$.

An experimental setup has been constructed according to the theoretical model, and the scheme is shown in Fig. 2.2(b). The samples of inner and outer masses are placed horizontally in an air track. Each unit is made of three blocks of length 30 mm, the first and last blocks are fixed together and the middle one is free to move. The three blocks are connected to each other by two soft springs with the same spring constant 37 N/m. The weights of the inner and outer masses are 46.47 g and 101.10 g, respectively. Figure 2.3(a) shows the effective mass m_{eff} (solid line) and dispersion curve qL (dashed line) as the function of frequency in the case of the free inner mass. It is seen that waves are forbidden in the frequencies of negative effective mass due to the decaying wave field amplitudes. Note that the resonance introduces not only negative effective mass but also extremely large mass just below ω_1. The large mass could result in strong spatial oscillation of wave fields within the periodic structures, giving rise to the Bragg gap. Notice that this low-frequency Bragg gap might be different from the common one in the sense that the Bragg resonance is occurring in the sub-

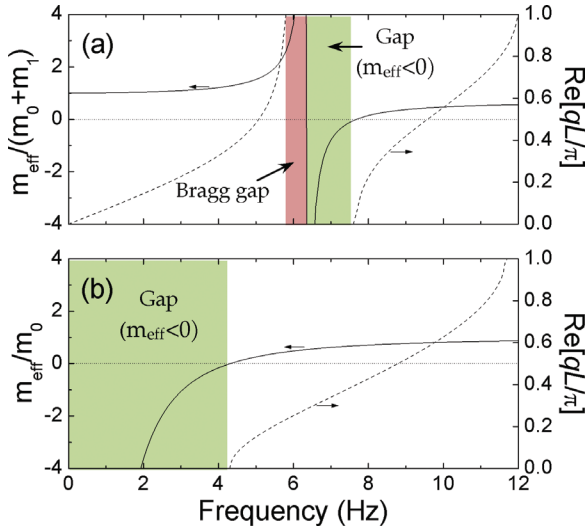

Figure 2.3 The effective mass and dispersion curve in the case of the free inner mass (a) and the fixed inner mass (b).

wavelength scale of metamaterials. When the inner mass is fixed, Fig. 2.3(b) shows that negative effective mass occurs below the cut-off frequency 4.3 Hz and opens a large gap region in the dispersion curve. Figures 2.4(a) and (b) present the experimental results of the transmission T of the lattice system comprising seven units in the case of free and fixed inner mass respectively. As a comparison, the transmission predicted in theory by Eq. (2.8) is also depicted. Both theoretical and experimental results demonstrate the transmission drop at frequencies of negative effective mass.

With help of the mass–spring model shown in Fig. 2.1(a) with either free or fixed inner mass, one is well equipped to understand the underlying physics of the negative effective mass exhibited in existing metamaterials. For example, metamaterials proposed by Liu *et al.* [9] consist of lead particles with the coating of the soft rubber embedded in an epoxy matrix. The lead particle, the rubber coating, and the epoxy matrix behave in the similar manner to the inner mass m_1, the spring G, and the outer mass m_0 in the discrete system. The membrane-type metamaterials [30] consist of a circular elastic membrane with a small weight attached in the center and the outer

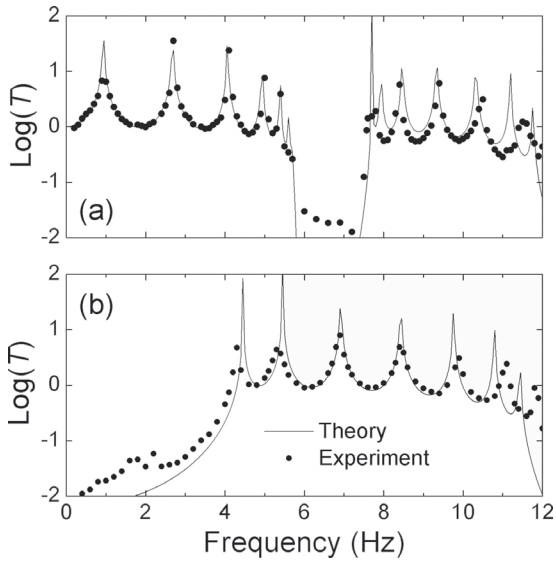

Figure 2.4 Transmission coefficients given by theory and experiment in the case of the free inner mass (a) and the fixed inner mass (b).

boundary being fixed. The small weight, the elastic membrane, and the ambient fluid respond to sound waves as the inner mass m_1, the spring G, and the outer mass m_0, respectively.

Lee *et al.* [15] propose that a stretched rubber membrane with the fixed outer boundary can be homogenized as an acoustic metamaterial with negative effective mass below a critical frequency. The physics can be understood by the mass–spring model with the fixed inner mass. In this case, the lattice system equivalent to Fig. 2.1(b) with the fixed inner mass is depicted in Fig. 2.5. It has been discovered that a rectangular solid waveguide with clamped boundary conditions may have dispersion characteristics similar to that of the lattice system, and the mass density, Young's modulus, and shear modulus of the solid material can realize m, K, and G of the lattice system, respectively [16]. As a simple demonstration, consider a two-dimensional waveguide filled by an elastic material and infinitely extended in the out-of-plane direction. When the waveguide has clamped boundary conditions, the dispersion relations are expressed as

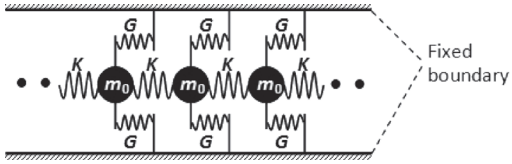

Figure 2.5 The lattice system corresponding to Fig. 2.1(b) in the case of the fixed inner mass.

$$\omega^2/\omega_d^2 = m^2 + \zeta^2, m = 1, 2, \ldots \tag{2.10a}$$

for P waves and

$$\omega^2/\omega_s^2 = n^2 + \zeta^2, n = 1, 2, \ldots \tag{2.10b}$$

for SV waves, where $\zeta = qh/\pi$, $\omega_d = \pi v_d/h$, $\omega_s = \pi v_s/h$, h is the width of the waveguide, v_d and v_s are respectively the wave velocities of longitudinal and shear waves, and q is the propagation constant along the wave-guiding direction. For conventional elastic materials, the shear wave velocity is always less than longitudinal wave velocity, which means that $\omega_s < \omega_d$. Therefore the dispersion relation (2.10) gives a lowest cut-off frequency ω_s for such waveguide, below which both P and SV waves are not allowed since the non-dimensional propagation constant ζ will be purely imaginary. Consider the general dispersion relation $(q/\omega)^2 = \rho_{\text{eff}}/\mu$, where μ is the shear modulus of the filling material. Let n be equal to 1 in Eq. (2.10b), the effective mass density ρ_{eff} for the waveguide with the clamped boundary condition is derived as

$$\rho_{\text{eff}} = \rho\left(1 - \frac{\omega_s^2}{\omega^2}\right) \tag{2.11}$$

where ρ is the mass density of the filling material. It is found that the bandgap effect below the cut-off frequency ω_s can be attributed to negative effective mass. Detailed analyses on negative effective mass below a cut-off frequency can be found in Ref. [16]. From Eq. (2.11), the cut-off frequency is related to the shear property of the solid material. Since the elastic membrane used in Lee's model does not resist shear deformations, it is the prestress applied on the stretched membrane that plays the role of the effective "shear" resistance.

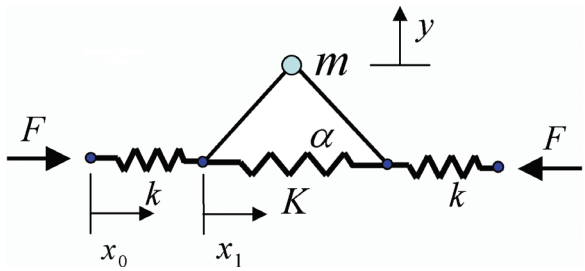

Figure 2.6 The mass–spring model of describing negative effective stiffness.

2.2.2 *Negative Effective Modulus*

The negative effective bulk modulus was first demonstrated in a hollow waveguide attached by an array of subwavelength Helmholtz resonators [10]. The negative effective modulus of elastic metamaterials is distinct from the negative static stiffness observed in the buckling state of compressed structures [31]; the former is induced by the locally resonant effects and can be stable without constraint. The effective compliance of Helmholtz resonators, i.e., the inverse of effective modulus, is found to have the Lorentz-type expression, showing an interesting correlation with the effective permeability of magnetic resonators [3]. This analogy enables one to understand the negative modulus from a simple inductor–capacitor circuit. Here a mass–spring model [32] is used to explore the underlying physics of negative effective stiffness, as shown in Fig. 2.6. In the model, three massless springs with spring coefficients k and K are connected, and a rigid sphere of weight m is attached to the middle spring by two massless rigid bars with the slope angle α. All joints are free of friction and the springs are confined in the horizontal direction.

Suppose that the time harmonic force $F(t)$ is applied symmetrically to the left and right boundaries of the model, and x_0, x_1, and y denote the offset of the end, middle joint and mass from the equilibrium position. From the equilibrium equation of the mass m, the following is obtained:

$$2(F - 2Kx_1)\tan\alpha = -m\omega^2 y \tag{2.12}$$

where $F = k(x_0 - x_1)$. In the case of infinitesimal deformation, the geometrical relation $x_1 = y\tan\alpha$ exists. The effective stiffness

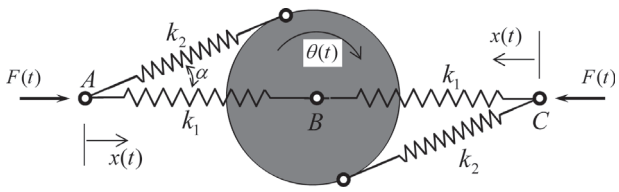

Figure 2.7 The mass–spring model of explaining negative effective modulus due to rotational resonances.

is defined to be $K_{\text{eff}} = F/(2x_0)$. From Eq. (2.12), the following is obtained:

$$\frac{1}{K_{\text{eff}}} = \frac{2}{k}\left(1 - \frac{\omega_0^2}{\omega^2 - \omega_1^2}\right) \tag{2.13}$$

where $\omega_1 = 2\tan\alpha\sqrt{K/m}$ and $\omega_0 = \tan\alpha\sqrt{2k/m}$. Equation (2.13) follows a typical Lorentz expression and predicts the negative effective stiffness to be between ω_1 and $\sqrt{\omega_1^2 + \omega_0^2}$. From Eq. (2.13), the negative effective modulus arises from the resonance between the mass m and spring K. The vertical oscillation of the sphere produces the additional inertial force in the horizontal vibration of the system. When the mass resonates, the system would have an expansion displacement under a compressive force, and vice versa. The Helmholtz cavities play the role of such mass–spring resonator. That is why the effective modulus of the waveguide with Helmholtz cavities could be negative. A solid continuum version of this mass–spring model has been recently proposed [33].

Based on the rotational resonance, chiral elastic metamaterials could exhibit the negative effective bulk modulus [12, 34]. The corresponding mass–spring model is proposed in Fig. 2.7. In the model, four massless springs and a rigid disk with rotational inertia I and radius R are pin-connected. Two springs with spring coefficients k_2 are tangential to the disk with an angle α. The pin joints A, B and C are kept in the horizontal axis. In the case of infinitesimal deformation, the force in the spring k_2 is $F_2 = k_2(R\theta - x\cos\alpha)$ when the system is symmetrically loaded by an equal force F. The equilibrium equation of the disk is written as $2F_2R = I\omega^2\theta$. The balance of forces at the pin joint A gives $F = k_1x - F_2\cos\alpha$. From above expressions, effective dynamic stiffness $K_{\text{eff}} = F/(2x)$

is derived to be

$$K_{\text{eff}} = \frac{k_1}{2} + \frac{k_2(\cos\alpha)^2}{2}\left(1 - \frac{\omega_0^2}{\omega_0^2 - \omega^2}\right) \tag{2.14}$$

where $\omega_0 = R\sqrt{2k_2/I}$. From Eq. (2.14), effective stiffness becomes negative in the frequency range between $\omega_0\sqrt{k_1/(k_1 + k_2\cos^2\alpha)}$ and ω_0. The corresponding continuum material model and the dynamic behaviors of chiral metamaterials will be discussed in the following section.

2.3 Continuum Material Model of Metamaterials

2.3.1 *Composites with Coated Sphere Inclusions*

Consider the propagation of elastic waves in composites of coated spheres embedded in a matrix. It has been found that negative effective mass arises from the dipolar resonance in composites with rubber-coated lead spheres suspended in the epoxy matrix. The negative effective bulk modulus is realized due to the monopolar resonance of bubble-contained-water spheres in an epoxy host. The negative effective shear modulus is designed when particles undergo the quadrapolar resonance. The physical reasons of negative effective parameters will be addressed here.

The analyzed model [13] is a coated sphere placed in an infinite matrix, as shown in Fig. 2.8. The building unit of the particulate composite is a doubly coated sphere with the outer radius given by $r_3 = r_2/\sqrt[3]{\phi}$, where ϕ is the filling fraction of the coated spheres. Each region of the doubly coated sphere is assumed to be elastic material characterized by mass density ρ_i, Lamé coefficients λ_i and μ_i, and volume fractions ϕ_i with the subscript $i = 1, 2, 3$ representing separately the sphere, the coating, and the matrix. Note that $\phi = \phi_1 + \phi_2$. Let r_1 denote the radius of the uncoated sphere and r_2 the radius of the coated sphere. A plane harmonic compressional wave propagates along the positive direction of the z axis. The general expressions of the scattering displacement and stress fields are [13]

$$u_r = \sum_n u_r'(r) P_n(\cos\theta) \tag{2.15a}$$

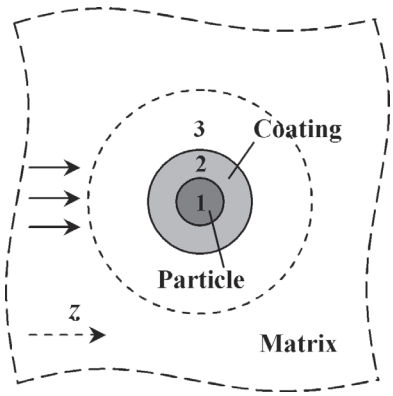

Figure 2.8 The analyzed model: a coated sphere placed in an infinite matrix.

$$u_\theta = \sum_n u'_\theta(r) \frac{d P_n(\cos\theta)}{d\theta} \tag{2.15b}$$

$$\sigma_{rr} = \frac{2}{r^2} \sum_n \sigma'_{rr}(r) P_n(\cos\theta) \tag{2.16a}$$

$$\sigma_{r\theta} = \frac{2}{r^2} \sum_n \sigma'_{r\theta}(r) \frac{d P_n(\cos\theta)}{d\theta} \tag{2.16b}$$

where $P_n(x)$ is the Legendre polynomial.

For a spherical volume V with the surface S and the radius R, the net force and total momentum are, respectively, given by

$$\vec{F} = \int_S d\vec{s} \cdot \tilde{\sigma} \tag{2.17}$$

$$\vec{P} = \int_V \vec{p} dv \tag{2.18}$$

where $\tilde{\sigma}$ is the stress tensor and $\vec{p}$ is the momentum. Consider the expression (2.16) of the scattering stress fields, the net force is not zero only in the incident direction $\vec{F} = F_z \vec{z}$. In addition, the net moment $\vec{M} = \int_s d\vec{s} \times \tilde{\sigma}$ is zero. Then the equilibrium equation of the sphere is expressed as

$$F_z = -i\omega p_z \tag{2.19}$$

The net force is given by

$$F_z(R) = 4\pi \sum_n \left[\sigma_{rr}(R) l_n + \sigma_{r\theta}(R) m_n\right] \tag{2.20}$$

where

$$l_n = \int_{-1}^{1} P_n(z) P_1(z) dz \tag{2.21a}$$

$$m_n = \int_{-1}^{1} P_n^1(z) P_1^1(z) dz \tag{2.21b}$$

Since the Legendre polynomials $P_n^m(z)$ are orthogonal functions, the only nonzero values in Eq. (2.21) are $l_1 = 2/3$ and $m_1 = 4/3$. The result means that only first-order (dipole) scattering fields contribute to the rigid-body motion of the sphere. Extend the results of Eqs. (2.19) and (2.20) to a doubly coated sphere, the total momentum p_z^i of each phase can be computed:

$$F_z(r_1) = -i\omega p_z^1 \tag{2.22a}$$

$$F_z(r_2) - F_z(r_1) = -i\omega p_z^3 \tag{2.22b}$$

$$F_z(r_3) - F_z(r_2) = -i\omega p_z^3 \tag{2.22c}$$

According to the homogenization method, effective mass ρ_{eff} can be defined as the total momentum of the doubly coated sphere divided by the velocity of the host material. It is then obtained that

$$\rho_{\text{eff}} = \phi_3 \rho_3 F_z(r_3)/[F_z(r_3) - F_z(r_2)] \tag{2.23}$$

It can be demonstrated that above definition coincides with that suggested by Eq. (2.4). In the long-wavelength limit, Eq. (2.23) reduces to the volume-averaged effective mass $\rho_{\text{eff}} = \sum \phi_i \rho_i$.

The averaged constitutive relation in a volume V is given by

$$\langle \tilde{\sigma} \rangle = 3\lambda \langle \varepsilon_{\text{b}} \rangle \tilde{I} + 2\mu \langle \tilde{\varepsilon} \rangle \tag{2.24}$$

where the averaging field $\langle \Gamma \rangle$ is defined as $\langle \Gamma \rangle = (1/V) \int_V \Gamma dv$, $\varepsilon_{\text{b}} = \text{tr}\tilde{\varepsilon}/3$ is the bulk strain and $\tilde{I}$ is the second-order identity tensor. The strain tensor $\tilde{\varepsilon}$ is related to the displacement field $\vec{u}$ by

$$\varepsilon_{\text{b}} = \frac{1}{3} \nabla \cdot \vec{u} \tag{2.25}$$

$$\tilde{\varepsilon} = \frac{1}{2}(\nabla\vec{u} + \vec{u}\nabla) \tag{2.26}$$

In each phase of the doubly coated sphere, the averaged bulk strain $\langle\varepsilon_{\mathrm{b}}\rangle_i$ is derived as

$$\langle\varepsilon_{\mathrm{b}}\rangle_1 = \frac{2\pi}{3V_1}\sum_n r_1^2 u_r'(r_1)s_n \tag{2.27a}$$

$$\langle\varepsilon_{\mathrm{b}}\rangle_2 = \frac{2\pi}{3V_2}\sum_n [r_2^2 u_r'(r_2) - r_1^2 u_r'(r_1)]s_n \tag{2.27b}$$

$$\langle\varepsilon_{\mathrm{b}}\rangle_3 = \frac{2\pi}{3V_3}\sum_n [r_3^2 u_r'(r_3) - r_2^2 u_r'(r_2)]s_n \tag{2.27c}$$

where

$$s_n = \int_{-1}^{1} P_n(z)P_0(z)dz \tag{2.28}$$

The only nonzero value in Eq. (2.28) is $s_0 = 2$, which reveals that the bulk deformation is dominated by the zero-order (monopole) scattering mode. The averaged bulk stress $\langle\sigma_{\mathrm{b}}\rangle = \langle\mathrm{tr}\tilde{\sigma}\rangle/3$ in the i-th region can be calculated by

$$\langle\sigma_{\mathrm{b}}\rangle_i = 3\kappa_i\langle\varepsilon_{\mathrm{b}}\rangle_i \tag{2.29}$$

where $\kappa_i = \lambda_i + 2\mu_i/3$ is the bulk modulus. According to the homogenization method, effective bulk modulus can be defined as the averaged bulk stress versus the averaged bulk strain in the doubly coated sphere

$$\kappa_{\mathrm{eff}} = \sum(\phi_i\kappa_i\langle\varepsilon_{\mathrm{b}}\rangle_i)\,/\,(\phi_i\langle\varepsilon_{\mathrm{b}}\rangle_i) \tag{2.30}$$

In the long-wavelength limit, Eq. (2.30) reduces to the static effective bulk modulus [31] for a doubly coated sphere assemblage.

In Eq. (2.24), the deviatoric part $\langle\tilde{\varepsilon}'\rangle_i$ of the averaging strain $\langle\tilde{\varepsilon}\rangle_i$ can be expressed as

$$\langle\tilde{\varepsilon}'\rangle_i = \varepsilon_i''\mathrm{diag}[-1, -1, 2] \tag{2.31}$$

where

$$\varepsilon_1'' = \frac{\pi}{3V_1}\sum_n r_1^2[2u_r'(r_1)p_n + u_\theta'(r_1)q_n] \tag{2.32a}$$

$$\varepsilon_2'' = \frac{\pi}{3V_2}\sum_n \left\{r_2^2[2u_r'(r_2)p_n + u_\theta'(r_2)q_n] - r_1^2[2u_r'(r_1)p_n + u_\theta'(r_1)q_n]\right\} \tag{2.32b}$$

$$\varepsilon_3'' = \frac{\pi}{3V_3}\sum_n \left\{r_3^2[2u_r'(r_3)p_n + u_\theta'(r_3)q_n] - r_2^2[2u_r'(r_2)p_n + u_\theta'(r_2)q_n]\right\} \tag{2.32c}$$

with

$$p_n = \int_{-1}^{1} P_n(z)P_2(z)dz \tag{2.33a}$$

$$q_n = \int_{-1}^{1} P_n^1(z)P_z^1(z)dz \tag{2.33b}$$

In Eq. (2.33), the non-vanishing values are $p_2 = 2/5$ and $q_2 = 12/5$. The result means that the shear deformation corresponds to the second-order (quadrapole) scattering mode. The averaged deviatoric stress $\langle\tilde{\sigma}'\rangle$ is related to the deviatoric strain through the shear modulus

$$\langle\tilde{\sigma}'\rangle_i = 2\mu_i\langle\tilde{\varepsilon}'\rangle_i \tag{2.34}$$

or equivalently,

$$\langle\tau\rangle_i = 2\mu_i\langle e\rangle_i \tag{2.35}$$

where the averaged (maximum) shear strain $\langle e\rangle_i$ is defined as $\langle e\rangle_i = 3\varepsilon_i''/2$, and $\langle\tau\rangle_i$ is the corresponding averaged (maximum) shear stress. The effective shear modulus can be defined as the averaged shear stress versus the averaged shear strain

$$\mu_{\text{eff}} = \sum(\phi_i\mu_i\langle e\rangle_i)/(\phi_i\langle e\rangle_i) \tag{2.36}$$

In the long-wavelength limit, Eq. (2.36) reduces to the static effective shear modulus [31] of a doubly coated sphere assemblage. So far, we have derived the effective mass density, bulk and shear modulus of a composite with coated particles embedded in a host material. In the following, we will discover by numerical results the physical mechanisms for the negative effective material parameters.

Consider the composite consisting of rubber-coated lead spheres embedded in an epoxy matrix. By use of Eqs. (2.22) and (2.23), Figs. 2.9(a) and 2.9(b) give effective mass density normalized

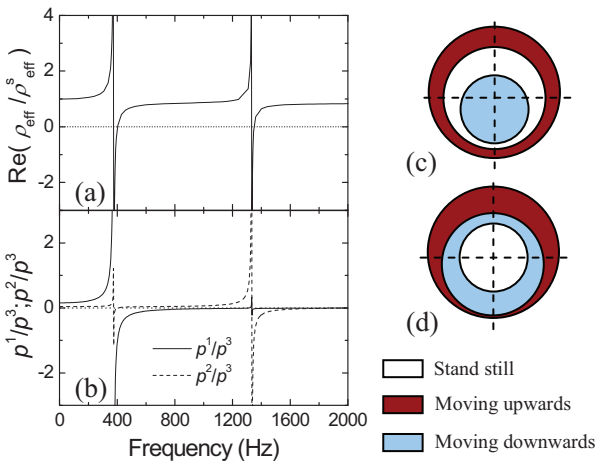

Figure 2.9 (a) Effective mass density, (b) the ratio of averaged momentums, and the schematic view of the displacement for a doubly coated sphere at frequencies associated with (c) the first and (d) the second negative-mass bands.

to the static one $\rho_{\text{eff}}/\rho_{\text{eff}}^{s}$ and the momentum ratios P^1/P^3 and P^2/P^3 between constituents. It is seen that there are two resonant negative-mass bands, with the lower and higher frequency bands induced respectively by the out-of-phase motions of the lead sphere and rubber coating with respect to the epoxy matrix, as shown schematically in Figs. 2.9(c) and 2.9(d). The physics disclosed here coincides with that discovered by a mass–spring structure.

For the composite of bubble-contained-water spheres embedded in an epoxy matrix Figures 2.10(a) and 2.10(b) give effective bulk modulus normalized to the static one $\kappa_{\text{eff}}/\kappa_{\text{eff}}^{s}$, and the averaged bulk strains $\varepsilon_i = \phi_i \langle \varepsilon_b \rangle_i$ of each constituents versus the total bulk strain $\varepsilon_{\text{total}} = \sum \varepsilon_i$. In Fig. 2.10(a), the composite exhibits a negative effective bulk modulus near the resonant frequency. To explore the physics for the negative bulk modulus, Fig. 2.10(c) shows the scheme of deformation profiles of the doubly coated sphere at the frequency of $\varepsilon_{\text{total}} > 0$, $\varepsilon_{\text{total}} < 0$, and $\varepsilon_{\text{total}} = 0$. The doubly coated sphere in the initial state without deformations is shown in the dashed line. When the composite sphere is in an expanded state, the inner core is expanded more due to the resonant effect so that the cover material

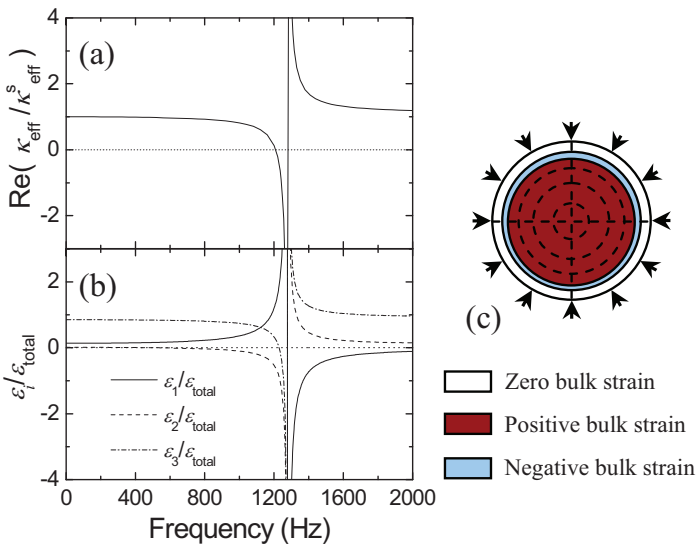

Figure 2.10 (a) Effective bulk modulus, (b) the averaged bulk strains of each constituent versus the total bulk strain, and (c) the schematic view of the deformation for a doubly coated sphere being in the expanded state. (The arrows indicate the directions of forces loading on the outermost surface of the composite sphere.)

is compressed and undergoing a compressive stress. Since the bulk modulus of water is much larger than that of air, the loading state of the composite sphere is governed by the water coating. This means that the composite sphere undergoes an expanding deformation under an external compressive stress. So the negative effective bulk modulus is defined to describe the out-of-phase volume deformation of local constituents with respect to the external triaxial loading.

Consider rubber-coated epoxy spheres embedded in a matrix of polyethylene foam. The effective shear modulus of the composite predicted by Eq. (2.36) is shown in Fig. 2.11(a). The method predicts a negative effective shear modulus in two narrow frequency bands. To understand the mechanism of the negative effective shear modulus, Fig. 2.11(b) plots the averaged shear strains $e_i = \phi\langle e\rangle_i$ of each constituent versus the total shear strain $e_{\text{total}} = \sum e_i$ as a function of frequency. The averaged shear strain of the matrix could become negative, in correspondence with the negative

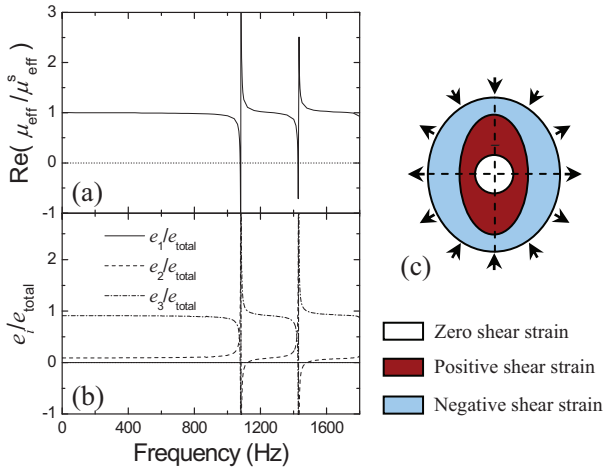

Figure 2.11 (a) Effective shear modulus, (b) the averaged shear strains of each constituent versus the total shear strain, and (c) the schematic view of the deformation for a doubly coated sphere with the prolate-shape deformation. (The arrows indicate the directions of forces loading on the outermost surface of the composite sphere.)

effective shear modulus. We simply assume that a sphere will become a prolate or oblate spheroid of the constant volume by the shear deformation. Figure 2.11(c) shows a schematic picture of the deformation profile of a doubly coated sphere at frequency of negative effective shear modulus. When the composite sphere (the outermost surface) is deformed with the prolate shape, the coating material also has a prolate shape but with a larger aspect ratio, as seen in Fig. 2.11(b). The inner core has no shear deformation at any frequency. So the matrix cover is actually compressed in the z direction and pulled in the x–y plane, macroscopically behaving as the oblate-shape deformation. Since the Polyethylene foam is stiffer than the soft rubber, the composite sphere will be under the same loadings to the polyethylene foam, denoted by the arrows in Fig. 2.11(c). The out-of-phase phenomenon between the deformation and the applied stress is the origin of negative effective shear modulus.

The above numerical results demonstrate that the out-of-phase effect induced by resonance is the origin of negative effective

material parameters. With help of the averaged physical fields, the analytic model provides a unified explanation for this unusual phenomenon. It is found that the first three scattering channels correspond, respectively to the rigid-body movement ($n = 1$), the volume (bulk) deformation ($n = 0$), and the axisymmetric (shear) deformation of a constant volume ($n = 2$). The negative effective mass is induced by the negative total momentum of the composite for a positive momentum excitation. The negative effective bulk modulus appears for composites with an increasing (decreasing) total volume under a compressive (tensile) stress. The negative effective shear modulus describes composites with axisymmetric deformation under an opposite axisymmetric loading.

2.3.2 *Chiral Metamaterials*

In Section 2.2.2, the mass–spring structure with rotational resonances has been demonstrated to exhibit negative effective modulus. The corresponding continuum material model is shown in Fig. 2.12, where the unit cell is composed of a heavy cylindrical core with soft coating embedded in a matrix, and a number of (n_s) slots with width t_s are cut out from the coating material. The slots are equi-spaced in azimuth and oriented at an angle θ_s with respect to the radial direction. Due to the fact that the slots in the coating are not oriented toward the center, the unit cell lacks in any planes of mirror symmetry, leading to the macroscopic chirality of metamaterials [12, 34]. For the three-component metamaterial without the slots, the negative effective mass can be produced due to the translational resonance of the core, and the rotational resonance can never happen. However, by introducing a chiral microstructure, the rotational resonance may be coupled to the overall dilatation of the unit cell and result in negative effective bulk modulus. With an appropriate design of the unit cell, it is anticipated to achieve both types of resonance in an overlapped frequency range, and hence the double negativity is achieved.

To evaluate the effective dynamic properties of the chiral metamaterial, the global stress Σ, strain E, resultant force F, and acceleration $\ddot{U}$ are averaged on the external boundary of the unit

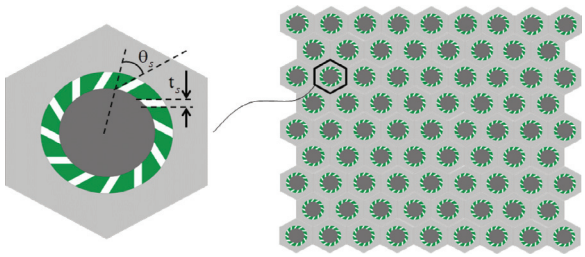

Figure 2.12 The chiral metamaterial.

cell [12]:

$$\Sigma_{\alpha\beta} = \frac{1}{V}\int_{\partial V} \sigma_{\alpha\gamma} x_\beta ds_\gamma \quad E_{\alpha\beta} = \frac{1}{2V}\int_{\partial V} \left(u_\alpha ds_\beta + u_\beta ds_\alpha\right)$$
$$F_\alpha = \frac{1}{V}\int_{\partial V} \sigma_{\alpha\beta} ds_\beta \quad \ddot{U}_\alpha = \frac{1}{S}\int_{\partial V} \ddot{u}_\alpha ds \tag{2.37}$$

where $\alpha, \beta, \gamma = 1, 2$, $\sigma_{\alpha\beta}$, u_α and $\ddot{u}_\alpha$ are the local stress, displacement and acceleration fields, respectively, $ds_\alpha = n_\alpha ds$ with n_α denoting the unit vector normal to the boundary, x_α is the position vector, V and ∂V denote the volume and external boundary of the unit cell, respectively. When the unit cell is periodically arranged in the triangular lattice with the lattice constant α, the metamaterials are isotropic near the Γ point in the wave vector space [35]. In such case, the effective bulk, shear modulus and mass density can be defined as

$$K_{\text{eff}} = \frac{1}{2}\Sigma_{\alpha\alpha}/E_{\alpha\alpha} \quad \mu_{\text{eff}} = \frac{1}{2}\Sigma'_{\alpha\beta}/E'_{\alpha\beta} \quad \rho_{\text{eff}} = F_\alpha/\ddot{U}_\alpha \tag{2.38}$$

where $\Sigma'_{\alpha\beta}$ and $E'_{\alpha\beta}$ are the deviatoric parts of the global stress and strain, respectively.

As an example, Fig. 2.13 shows effective mass, effective modulus, and the dispersion curves along ΓK direction of the chiral metamaterial. In Fig. 2.13(a), it is seen that negative effective mass is realized, which arises from the translational resonance between the inner particle and soft coating. In addition, effective bulk modulus also becomes negative due to the rotational resonance, as shown in Fig. 2.13(b). To clearly illustrate the mechanism of negative effective bulk modulus, the deformation profiles of the unit cell are plotted

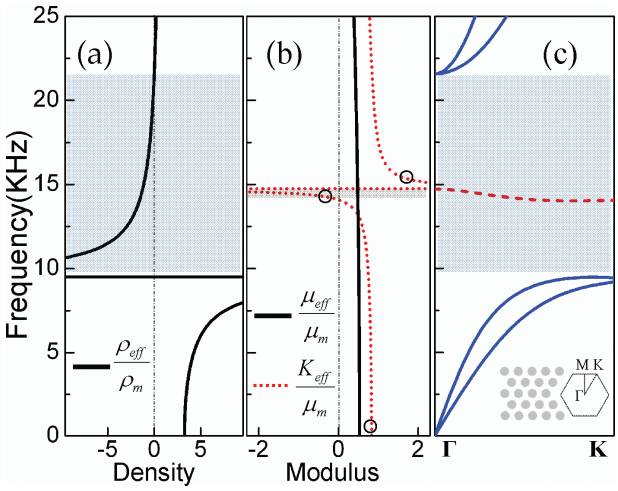

Figure 2.13 (a) Effective mass, (b) bulk modulus, and (c) band structure of the chiral elastic metamaterial.

in Fig. 2.14, for three typical values of K_{eff} as marked in Fig. 2.13(b) by black circles. In the figures, the undeformed shapes are shown in the dashed lines, and the boundary tractions are depicted by arrows. In the quasi-static frequency (Fig. 2.14(a)), $K_{\text{eff}} > 0$ and the unit cell is expanded by the tensile stress. Figure 2.14(b) shows the result of $K_{\text{eff}} < 0$, where the inner core rotates in-phase with the overall deformation so that a very large clockwise

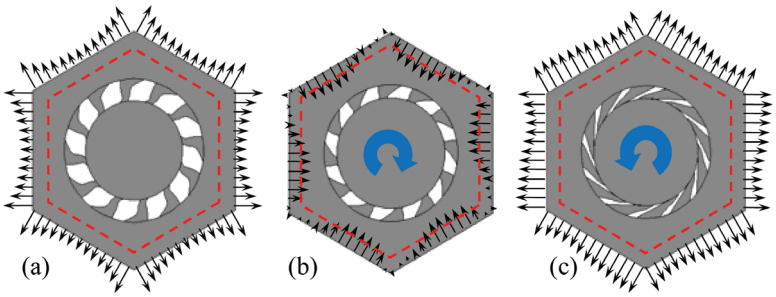

Figure 2.14 The deformation profile of the unit cell in three cases as highlighted in Fig. 2.13(b) by black circles: (a) quasi-static frequency; (b) $K_{\text{eff}} < 0$: (c) $K_{\text{eff}} > 0$.

rotation is generated in conjunction with an expanded unit cell. The compressive stress needs to be produced in the matrix to balance the pressure exerted by such a rotation, as the result of negative effective bulk modulus. Above the rotational resonance frequency where $K_{\text{eff}} > 0$, Fig. 2.14(c) shows that the anti-clockwise rotation of the core produces the tensile stress in the matrix and, consequently a positive effective modulus is defined.

The dispersion curves along ΓK direction in the triangular lattice system are shown in Fig. 2.13(c). It is seen that at the frequencies where only effective mass is negative, the dispersion curve shows a bandgap. Among the gap region, a pass band with negative phase velocity is produced when effective longitudinal modulus $E_{\text{eff}} = K_{\text{eff}} + \mu_{\text{eff}}$ also becomes negative. Metamaterials with simultaneous negative values of effective mass and effective modulus are often termed as double-negative or left-handed metamaterials [36]. The "left-handed" is termed because of their electromagnetic (EM) counterpart with negative effective permittivity and negative effective permeability, for which the electric field, the magnetic field and the wave vector would follow the left-handed rule [1], instead of the right-handed one for conventional materials. The double-negative metamaterials have negative refractive index, meaning that the transmitted wave will be refracted toward the same side of the incident wave. Figure 2.15 shows the result of negative refraction by a double-negative chiral metamaterial [12]. The wedged sample with the slope angle 30° consists of 546 unit cells with a triangular array and is immersed in water. A Gaussian acoustic pressure beam is launched from the bottom side of the sample. Figure 2.15(a) shows the contour plot of acoustic pressure fields at the designed frequency 14.53 kHz, where effective bulk, shear modulus and mass density of the metamaterial are evaluated to be -1.58 GPa, 0.42 GPa, and –1481 kg/m^3 respectively. It can be clearly seen that the energy flux of the refraction wave outside of the sample travels on the negative refraction side of the surface normal. Figure 2.15(b) shows the result in a left-sloped wedge with the same microstructural chirality at the same frequency. It is interesting to find almost the same negative refraction phenomenon in spite of the chirality.

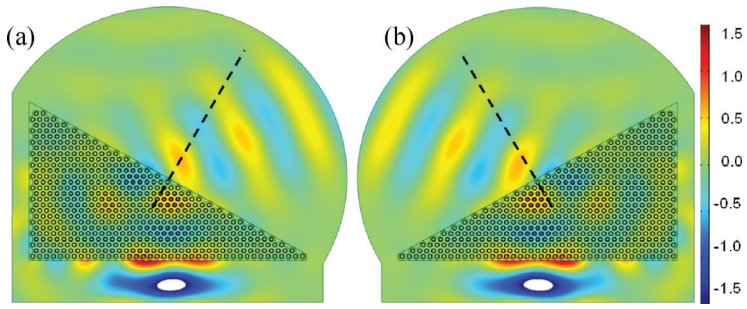

Figure 2.15 Simulation results of negative refraction. (a) The incident beam is negatively refracted in the right-sloped wedge at frequency 14.53 kHz. (b) The incident beam is negatively refracted in the left-sloped wedge at frequency 14.53 kHz.

2.4 Applications of Elastic Metamaterials

The metamaterials offer a great choice on material selection for wave manipulations. One of the most interesting applications of metamaterials is the "invisibility cloaking" for electromagnetic or elastic waves. The cloak can render an object undetectable by waves, which may find important applications in stealth technology. There are two techniques for metamaterials to render an object undetectable: the first one is based on wave cancellation mechanism [37–40] and the other is relying on the transformation method [41–43], by which waves are guided to go around an object without scatterings. Both methods will be discussed in the following two subsections. Application of metamaterials to acoustic superlens will be presented in the third subsection.

2.4.1 *Cloaking in Quasi-Static Approximation*

The cancellation mechanism for electromagnetic waves is proposed by Alu and Engheta [37], who utilize a plasmonic or metamaterial coating to cover a spherical or cylindrical dielectric core. By adjusting the material and geometrical parameters, they found that at certain configuration, the total scattering cross section of this coated sphere can be extremely low. Zhou and Hu [38] have extended the transparency phenomenon to multilayered sphere,

coated spheroids and two-phase composites by introducing the "neutral inclusion" concept. Afterwards the idea is further extended to the regime of acoustic [39] and elastic [40] waves. Consider an inclusion of random shape is put into an infinite matrix. The inclusion is characterized by the bulk modulus κ_*, shear modulus μ_*, mass density ρ_*, and the infinite matrix has the material parameters κ_0, ρ_0, and ρ_0. The inclusion can be made of either a homogeneous medium or a heterogeneous material. For the latter, κ_*, μ_*, and ρ_* then denote the effective material parameters of the heterogeneous material (i.e., the inclusion). When the material properties of the inclusion are the same as those of the background medium, the wave fields outside of this inclusion will not be disturbed. In other word, the inclusion will not be "seen" by an outside observer and become undetectable. This is the basic idea of the "neutral inclusion" concept. When the region is made of a homogeneous material, this is a trivial case. However, if the region is made of a heterogeneous material, there are many design possibilities for equating its effective material property to that of the background medium. According to the neutral inclusion concept, the key point to achieve transparency is to determine the effective parameters of the (heterogeneous) inclusion, or to find an equivalent homogeneous medium for the inclusion.

In the quasi-static approximation, heterogeneous materials can be described by equivalent homogeneous ones based on the homogenization technique. In this approximation, a neutral inclusion can be a simple pattern (coated sphere, coated spheroid, etc.). When a neutral inclusion is embedded in a material made of assemblages of such pattern with gradual sizes (in order to fill the whole space), it will not perturb the static stress fields outside of this inclusion [44]. Although the neutral inclusion is defined in the quasi-static case, it can still help to realize transparency in the full-wave scattering case when the wavelength becomes comparable to the size of the inclusion [45]. The elastic wave transparency of a solid sphere coated with metamaterials will be exemplified here, and the neutral inclusion concept is explained by analyzing the scattering of a coated sphere.

Consider a coated sphere immersed in a matrix. Material parameters are bulk modulus κ_i, shear modulus μ_i, and mass

density ρ_i, with the subscript $i = 1, 2, 3$ representing separately the sphere, the coating, and the host medium. Let r_1 denote the radius of the uncoated sphere and r_2 the radius of the coated sphere. A plane harmonic compressive wave is incident on the coated sphere. The total scattering cross section Q_{sca} of the coated sphere can be expressed as [40]

$$Q_{\text{sca}} = \lambda_3^2 \sum_{n=0}^{\infty} \frac{1}{(2n+1)\pi} \left[|a_n|^2 + n(n+1)\frac{\alpha_3}{\beta_3}|b_n|^2 \right] \tag{2.39}$$

where α_3 and β_3 are propagating constants of longitudinal and transverse waves, respectively. $\lambda_3 = 2\pi/\alpha_3$ is the wavelength of the compressive wave in the host medium, α_n and b_n are the unknown scattering coefficients of scattered waves. In the Rayleigh approximation, the first three scattering coefficients are given below for different configurations classified by the solid and fluid nature of materials.

Case I: Solid coating and solid host materials

$$\begin{aligned}
a_0 &= i\frac{\kappa_{\text{eff}}^{\text{HS}} - \kappa_3}{3\kappa_{\text{eff}}^{\text{HS}} + 4\mu_3}(\alpha_3 r_2)^3, \quad a_1 = \frac{\rho_{\text{eff}}^{\text{M}} - \rho_3}{3\rho_3}(\alpha_3 r_2)^3 \\
a_2 &= -\frac{20i\mu_3(\mu_{\text{eff}}^{\text{HS}} - \mu_3)/3}{6\mu_{\text{eff}}^{\text{HS}}(\kappa_3 + 2\mu_3) + \mu_3(9\kappa_3 + 8\mu_3)}(\alpha_3 r_2)^3 \\
b_1 &= -\frac{\rho_{\text{eff}}^{\text{M}} - \rho_3}{3\rho_3}\alpha_3\beta_3^2 r_2^3, \\
b_2 &= \frac{10i\mu_3(\mu_{\text{eff}}^{\text{HS}} - \mu_3)/3}{6\mu_{\text{eff}}^{\text{HS}}(\kappa_3 + 2\mu_3) + \mu_3(9\kappa_3 + 8\mu_3)}(\beta_3 r_2)^3
\end{aligned} \tag{2.40}$$

Case II: Fluid coating and solid host materials

$$\begin{aligned}
a_0 &= i\frac{\kappa_{\text{eff}}^{\text{HS}} - \kappa_3}{3\kappa_{\text{eff}}^{\text{HS}} + 4\mu_3}(\alpha_3 r_2)^3, \quad a_1 = \frac{\rho_{\text{eff}}^{\text{B}} - \rho_3}{3\rho_3}(\alpha_3 r_2)^3, \\
a_2 &= \frac{20i\mu_3}{3(9\kappa_3 + 8\mu_3)}(\alpha_3 r_2)^3, \\
b_1 &= -\frac{\rho_{\text{eff}}^{\text{B}} - \rho_3}{3\rho_3}\alpha_3\beta_3^2 r_2^3, \quad b_2 = -\frac{10i\mu_3}{3(9\kappa_3 + 8\mu_3)}(\beta_3 r^2)^3
\end{aligned} \tag{2.41}$$

Case III: Solid coating and fluid host materials

$$a_0 = i\frac{\kappa_{\text{eff}}^{\text{HS}} - \kappa_3}{3\kappa_{\text{eff}}^{\text{HS}}}(\alpha_3 r_2)^3, \quad a_1 = \frac{\rho_{\text{eff}}^{\text{M}} - \rho_3}{2\rho_{\text{eff}}^{\text{M}} + \rho_3}(\alpha_3 r_2)^3 \tag{2.42}$$

Case IV: Fluid coating and fluid host materials

$$a_0 = i\frac{\kappa_{\text{eff}}^{\text{HS}} - \kappa_3}{3\kappa_{\text{eff}}^{\text{HS}}}(\alpha_3 r_2)^3, \quad a_1 = \frac{\rho_{\text{eff}}^{\text{B}} - \rho_3}{2\rho_{\text{eff}}^{\text{B}} + \rho_3}(\alpha_3 r_2)^3 \tag{2.43}$$

In every case, the parameter b_0 is not important and thus not given here. In Eqs. (2.40)∼(2.43), the parameters $\kappa_{\text{eff}}^{\text{HS}}$, $\mu_{\text{eff}}^{\text{HS}}$, $\rho_{\text{eff}}^{\text{M}}$ and $\rho_{\text{eff}}^{\text{B}}$ have been used, which are

$$\kappa_{\text{eff}}^{\text{HS}}/\kappa_2 = 1 + \frac{c_1(\kappa_1 - \kappa_2)}{\kappa_2 + (1 - c_1)p(\kappa_1 - \kappa_2)} \tag{2.44}$$

$$\mu_{\text{eff}}^{\text{HS}}/\mu_2 = 1 + \frac{c_1(\mu_1 - \mu_2)}{\mu_2 + (1 - c_1)q(\mu_1 - \mu_2)} \tag{2.45}$$

with $p = \frac{3\kappa_2}{3\kappa_2 + 4\mu_2}$ and $q = \frac{6}{5}\frac{\kappa_2 + 2\mu_2}{3\kappa_2 + 4\mu_2}$,

$$\rho_{\text{eff}}^{M}/\rho_2 = 1 + c_1\frac{\rho_1 - \rho_2}{\rho_2} \tag{2.46}$$

$$\rho_{\text{eff}}^{B}/\rho_2 = +\frac{3c_1(\rho_1 - \rho_2)}{3\rho_2 + 2(1 - c_1)(\rho_1 - \rho_2)} \tag{2.47}$$

where $c_1 = (r_1/r_2)^3$. For a composite filled with coated spheres that are randomly distributed in the host medium and have gradual sizes in order to fill the whole space, $\kappa_{\text{eff}}^{\text{HS}}$ and $\mu_{\text{eff}}^{\text{HS}}$ denote effective bulk modulus and effective shear modulus of the composite calculated with the Hashin–Shtrikman (HS) bound. $\rho_{\text{eff}}^{\text{M}}$ is the effective mass density obtained by the volume averaged method, whereas $\rho_{\text{eff}}^{\text{B}}$ is the effective mass density calculated with Berryman's formula. With help of above effective parameters, Equations (2.40)∼(2.43) represent also the solutions of a single sphere having the material parameters $\kappa_{\text{eff}}^{\text{HS}}$, μ_{eff}^{M}, $\rho_{\text{eff}}^{\text{M}}$ (or $\rho_{\text{eff}}^{\text{B}}$) embedded in the host material. This implies that in the Rayleigh limit a coated sphere can be equivalent to a homogeneous effective sphere, and the coated sphere and its effective sphere has almost the same scattering fields in the host medium.

Based on Eqs. (2.40)∼(2.43), the transparency phenomenon of a coated sphere can be investigated systematically by reducing the scattering coefficients. If the effective parameters satisfy $\kappa_{\text{eff}}^{\text{HS}} = \kappa_3$, $\mu_{\text{eff}}^{\text{HS}} = \mu$, and $\rho_{\text{eff}}^{M} = \rho_3$ for a solid coating or $\rho_{\text{eff}}^{B} = \rho_3$ for a fluid coating, the scattering coefficients of the first three orders

are greatly minimized in the Rayleigh limit. In this case, an outside observer can hardly detect the coated sphere from the scattered waves it receives. Physically, the above transparency conditions can be directly obtained by the neutral inclusion concept. A coated sphere can be represented by its effective sphere in the long wavelength approximation, then the transparency conditions are obtained by equating the effective parameters of the coated sphere to those of the surrounding medium. This is exactly the physical meaning of the neutral inclusion concept.

As an example, a fluid cover can be designed to cloak an aluminum sphere of radius $r_1 = \lambda_3/5$ immersed in water. According to the transparency conditions, the cloaking material should have material parameters $\kappa_2 = 0.58\kappa_3$ and $\rho_2 = 0.55\rho_3$. However, the effectiveness of this cover lies within the Rayleigh limit. For the case of $r_1 = \lambda_3/5$, the parameters for a minimized value of the scattering may be further tuned to the desirable values of $\kappa_2 = 0.47\kappa_3$ and $\rho_2 = 0.4\rho_3$ by varying κ_2 and ρ_2 around the target values of $\kappa_2 = 0.58\kappa_3$ and $\rho_2 = 0.55\rho_3$. Materials with these optimized parameter combinations are not readily available in nature, but can be purposely fabricated with an acoustic metamaterial. Figures 2.16(a) and 2.16(b) present the near field contour plots of the radial component of the scattered displacement fields for an uncoated aluminum sphere and that with an optimized cloak, respectively. It can be seen that the uncoated sphere produces strong and

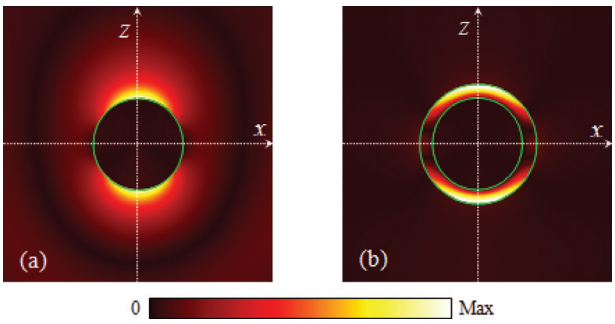

Figure 2.16 Contour plots of radial component of scattered displacement field for (a) uncoated aluminum sphere, and (b) the same sphere with the cloak.

nonuniform scattering field in the matrix, especially in the region adjacent to the sphere. However, when the cloaking material covers the sphere, the scattering is dramatically reduced whilst the field strength within the cloak is large. In the both cases, the displacement field inside the aluminum sphere is negligibly small due to its large modulus. It is thus demonstrated that, with the cloaking material, the impenetrable sphere can indeed achieve acoustic transparency. This property of the composite system can lead to potential applications in underwater stealth technology.

2.4.2 *Transformation Acoustics and Elasticity*

In contrast to the wave cancellation mechanism, the method to render an object undetectable by guiding waves around an object without scatterings is based on the coordinate transformation, and has been termed as transformation optics, acoustics or elasticity, applying respectively to electromagnetic, acoustic, or elastic waves. Transformation method solves an inverse problem, and derives spatial distributions of material parameters from desired wave propagation. The basic idea of transformation methods generalized by Greenleaf *et al.* [43], Pendry *et al.* [42] and Leonhardt [41] is based on the form-invariance of Maxwell or Helmholtz equations under a general coordinate transformation, and such a topological effect in spatial mapping can be mimicked by spatial distribution of materials. To proceed, the general expression of Helmholtz equation involving anisotropic mass is written as

$$(\rho_{ij}^{-1} p_i)_j = -\frac{\omega^2}{\kappa} p \tag{2.48}$$

where p is the sound pressure, κ is the bulk modulus, ρ_{ij} is the mass tensor. Consider a mapping from an initial space to a curvilinear space $x \to x'$. In the new space (x′), Eq. (2.48) is transformed to

$$A_i^{j'} (\rho_{ij}^{-1} A_i^{i'} p_{i'})_{j'} = -\frac{\omega^2}{\kappa} p \tag{2.49}$$

where $A_i^{i'} = \partial x'_{i'}/\partial x_i$ is the Jacobin matrix describing the coordinate transformation from x to x′. Introduce the Jacobian $J = \det(A)$ and consider the relation $(J^{-1} A_j^{j'})_j = 0$ [46], Eq. (2.49) can be further

expressed as

$$(\rho'^{-1}_{i'j'}\, p_{j'})_{j'} = -\frac{\omega^2}{\kappa'}\, p \tag{2.50}$$

with

$$\rho'^{-1}_{i'j'} = j^{-1} A^{i'}_{i} A^{j'}_{j}\, \rho^{-1}_{ij} \quad \kappa' = J\,\kappa \tag{2.51}$$

It is found that Eq. (2.50) has the same form to Eq. (2.48), meaning that the topological change under the mapping can be mimicked by the changed materials parameters $\rho'_{i'j'}$ and κ'. From Eq. (2.51), material parameters can be uniquely determined for a specific space mapping. As an example, the space mapping for a cylindrical cloak that guides waves around an object is written as

$$r' = a + r(a-b)/b, \quad \theta' = \theta \tag{2.52}$$

where r and θ are polar coordinates, and a and b are, respectively, the inner and outer radii of the cloak. From Eq. (2.51), the mass density and modulus of the acoustic cloak are

$$\rho'_r = \rho\frac{r'}{r'-a}, \quad \rho'_\theta = \rho\frac{r'-a}{r'}, \quad \kappa' = \kappa\left(\frac{b-a}{b}\right)^2 \frac{r'}{r'-a} \tag{2.53}$$

Figure 2.17 shows the contour plot of pressure fields of a plane wave incident leftwards on a rigid cylinder without and with the cloak. It is seen that a shadow is left behind the uncloaked cylinder (Fig. 2.17(a)), while the cloak could guide the incoming wave around the object with any scatterings, as if there is nothing there (Fig. 2.17(b)). The mass density and modulus of the cloak are very difficult to be realized by conventional materials. Metamaterials with designable material parameters offer us a good candidate serving for transformation materials. A prototype of acoustic cloak made of Helmholtz resonators has been designed and validated by experiments [47].

In reality, the cloaks or other transformation devices may have irregular geometries and the space mapping is difficult to construct analytically. To circumvent this difficulty, much effort has been made to derive material parameters for various kinds of irregular cloaks. As a general approach, Hu *et al.* [48] develop a deformation-based method to design transformation materials with arbitrary geometries. In this method, the Jacobin matrix $\tilde{A}$ represents the

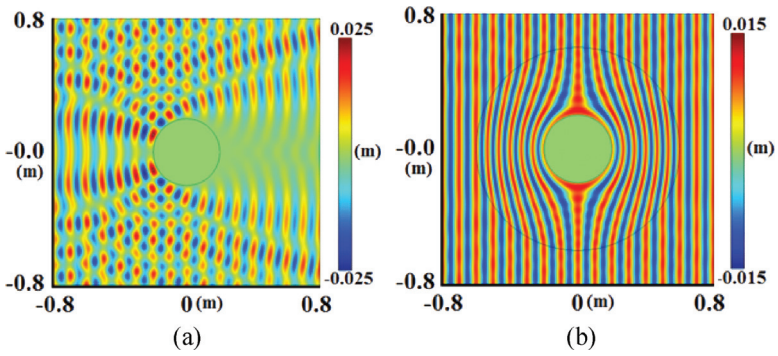

Figure 2.17 Contour plots of pressure field distributions of a plane wave incident on a rigid cylinder (a) without and (b) with the cloak. ($a = 0.2$ m, $b = 0.6$ m, $\rho = \kappa = 1$ for the background material.)

displacement gradient and can be locally decomposed into a rigid-body rotation $\tilde{R}$ and a stretch operation $\tilde{V}$, i.e., $\tilde{A} = \tilde{R}\tilde{V}$. Consider $\tilde{R}\tilde{R}^T = \tilde{I}$ and $\tilde{V} = \text{diag}[\lambda_1, \lambda_2, \lambda_3]$, $J = \det(\tilde{A}) = \lambda_1, \lambda_2, \lambda_3$ where λ is the principle stretch of the deformation tensor. Equation (2.51) is rewritten as

$$\tilde{\rho}' = \rho \text{diag}\left[\frac{\lambda_2\lambda_3}{\lambda_1}, \frac{\lambda_1\lambda_3}{\lambda_2}, \frac{\lambda_1\lambda_2}{\lambda_3}\right], \quad \kappa' = \kappa\lambda_1\lambda_2\lambda_3 \tag{2.54}$$

The mapping $x'(x)$ can be derived by solving the deformation field in a boundary value problem governed by the Laplace's equation $\Delta_x x' = 0$. The boundary conditions are defined according to the functionality of the device. As an example of a cloak bounded by inner and out boundaries a and b, the boundary conditions are written as

$$x'(0) = a, x'(b) = b \tag{2.55}$$

With help of a numerical solver, the material parameters of irregular cloaks can be easily obtained by solving the Laplace's equation with appropriate boundary conditions.

At the inner boundary $r' = a$ of a two-dimensional cloak, material parameters are often singular, for example $\rho'_r \to \infty$, $\rho'_\theta \to 0$, and $\kappa' \to \infty$ of the cylindrical cloak. These singular parameters are not readily realized in practice, therefore it is necessary to find a mapping without these singular points. In Eq. (2.54), the out-of-plane principal stretch λ_3 is a free parameter and can be used to

offset the infinite or near-zero in-plane principal stretch (λ_1 or λ_2), then singular material parameters can be removed [49]. The method can also be useful for other transformation materials to adjust the range of material parameters, and greatly reduce the difficulty of metamaterial fabrication.

The further study made by Chang *et al.* [50] shows that the inverse Laplace's equation $\Delta_{x'}x = 0$ with sliding boundary conditions (i.e., Neumann boundary conditions) will solve a quasi-conformal mapping as the result of minimizing the Winslow functional

$$F_W(x') = \frac{1}{2}\int_\Omega \left(\frac{g_{11}+g_{22}}{\sqrt{g}}\right) dx \tag{2.56}$$

where $g = \det(g_{ij})$, and $g_{ij} = [\tilde{V}\tilde{V}^T]_{ij}$. By use of the principle stretch λ_1, Eq. (2.56) is rewritten as

$$F_W(x') = \frac{1}{2}\int_\Omega \left(\frac{\lambda_1}{\lambda_2}+\frac{\lambda_2}{\lambda_1}\right) dx \tag{2.57}$$

So the inverse Laplace's equation results in the quasi-conformal mapping $\lambda_1 \approx \lambda_2$. Since the dilatational and shear deformations determine respectively the magnitude and anisotropy of the transformation material, quasi-conformal mapping will give nearly isotropic material parameters by keeping the grids as iso-volume as possible. It is due to the quasi-conformal mapping that the carpet cloaks [51, 52] have nearly isotropic parameters and are easier to fabricate compared to the cylindrical cloaks.

For elastic waves, Navier's equation in linear-elastic dynamics is written as

$$\frac{\partial \sigma_{ij}}{\partial x_j} = \rho\frac{\partial^2 u_i}{\partial t^2}, \sigma_{ij} = C_{ijkl}\frac{\partial u_k}{\partial x_l} \tag{2.58}$$

Under a general coordinate transformation, Navier's equation will be transformed into Willis' one [27]. Otherwise the form invariance is maintained only when the stiffness tensor C_{ijkl} losses the minor symmetry [53], and leading to the following asymmetric transformation relation

$$C'_{ijkl} = \frac{1}{J}A_j^{j'}A_l^{l'}C_{ijkl}, \rho' = \frac{1}{J}\rho \tag{2.59}$$

It is necessary to find a symmetric transformation relation to facilitate the design of transformation elastic materials. Regarding

this issue, the deformation-based transformation method suggested by Hu *et al.* [48] is further developed. In the local principal coordinate e_i' of $\tilde{V}$, where the principal stretch is λ_i, the governing equation in the transformed space is

$$\frac{\partial \sigma_{ij}'}{\partial x_j'} = \rho' \frac{\partial^2 u_i'}{\partial t^2}, \sigma_{ij}' = C_{ijkl}' \frac{\partial u_k'}{\partial x_l'} \tag{2.60}$$

where the physical fields and material parameters can be written as [28, 54]

$$\sigma_{ij}' = a_I a_J \sigma_{ij}, u_i' = b_I u_i, C_{ijkl}' = c_I c_J c_K c_L C_{ijkl}, \rho_{ij}' = d_I \delta_{ij} \rho \tag{2.61}$$

where a_i, b_i, c_i, and d_i are scaling factors remained to be determined, δ_{ij} is the Kronecker delta, and the capital letter in the index means the same value as its corresponding lowercase letter but without the summation. Equations (2.58) and (2.60) are related by the operator $\partial/\partial x_i' = \partial/\lambda_i \partial x_i$ in the approximation of local affine transformation. By the comparison between Eqs. (2.58) and (2.60), the following constraint relations are obtained for the scaling factors

$$\frac{a_I a_J}{\lambda_J} = d_I b_I, a_I a_J = c_I c_J c_K c_L \frac{b_K}{\lambda_I} \tag{2.62}$$

Consider the conservation of energy during the coordinate transformation at each element

$$\sigma_{ij}' \left(\frac{\partial u_i'}{\partial x_j'} + \frac{\partial u_j'}{\partial x_i'} \right) = \frac{1}{J} \sigma_{ij} \left(\frac{\partial u_i'}{\partial x_j'} + \frac{\partial u_j'}{\partial x_i'} \right) \tag{2.63a}$$

$$\rho' \frac{\partial^2 u_i'}{\partial t^2} = \frac{1}{J} \rho \frac{\partial^2 u_i}{\partial t^2} \tag{2.63b}$$

where the Jacobian J represents the volume change of the infinitesimal element in the local point x'. From Eq. (2.63), two additional constraint relations can be obtained

$$a_I a_J b_I = \frac{\lambda_i}{J}, d_I b_I = \frac{1}{J} \tag{2.64}$$

Combine Eqs. (2.62) and (2.64) to find the unique solution for elastic waves

$$a_i = \frac{\lambda_i}{\sqrt{J}}, b_i = \frac{1}{\lambda_i}, c_i = \frac{\lambda_i}{\sqrt[4]{J}}, d_i = \frac{\lambda_i^2}{J} \tag{2.65}$$

Finally, the transformation relations are

$$C'_{ijkl} = \frac{1}{J} A_i^{i'} A_j^{j'} A_k^{k'} A_l^{l'} C_{ijkl}, \rho' = \frac{1}{J} A_i^{i'} A_j^{j'} \delta_{ij} \rho \tag{2.66}$$

Note that transformation materials with the parameters (2.66) are within the framework of linear-elastic dynamics and potentially realizable by metamaterial technology. To derive Eq. (2.66), the local affine transformation is assumed to retain locally the form invariance of Navier's equation. Such approximation is pertinent when the deformation gradient is small or the size of the transformation material is sufficiently larger than the operating wavelength. It is also shown that the transformation relations Eq. (2.66) keep the eikonal equation invariant. i.e., the wave path can be controlled exactly, but leave the amplitude of the wave to be controlled approximately [28]. Based on the theory of transformation elasticity and elastic metamaterial technology, it is possible to control elastic waves, and many engineering applications could be anticipated.

2.4.3 *Acoustic Imaging beyond the Diffraction Limit*

Metamaterials could serve as acoustic lenses that create images with the spatial resolution beyond the diffraction limit. Acoustic images are obtained from the scattering fields of the objects under wave excitations. Among the scattered fields, evanescent wave components with large spatial frequency carry the object's subwavelength features. Due to the decaying nature in conventional materials, evanescent waves are permanently lost in the image region, resulting in the limited resolution of the imaging system. This is the well known diffraction limit [55], which defines the spatial resolution not smaller than half of the operating wavelength. To overcome the diffraction limit, it is necessary for the imaging system to interact with evanescent waves as the result of their amplitudes being enhanced or preserved.

For EM waves, Pendry [56] proposed the idea of using metamaterials with negative refractive index to overcome the diffraction limit by exciting surface waves. Since then, much efforts have been made to achieve the super-resolution imaging based on the metamaterial concept [57]. Ambati *et al.* [58] found that negative mass of metamaterials is the necessary condition to support surface

resonant states for acoustic waves. Consider a flat slab material of mass density ρ, modulus κ, and thickness h sandwiched between two semi-infinite fluid material of mass density ρ_0 and modulus κ_0. The surface resonant states represent the perturbations with pressures maximum at the interface and exponentially decaying in the direction perpendicular to the interface. By use of continuous conditions of pressure and normal velocity fields at the two interfaces, the conditions for surface states can be derived as

$$(\rho_0 k_x + \rho k_{0x})^2 = (\rho_0 k_x - \rho k_{0x})^2 e^{2ik_x h} \tag{2.67}$$

where $k_x^2 + k_y^2 = \omega^2 \rho/\kappa$ and $k_{0x}^2 + k_y^2 = \omega^2 \rho_0/\kappa_0$. For evanescent waves with spatial frequency $k_y > \omega\sqrt{\rho_0/\kappa_0}$, k_x takes purely imaginary values. When $h \to \infty$, $e^{2ik_x h} \to 0$. Equation (2.67) then reduces to the surface resonant condition at the interface of two semi-infinite fluid medium

$$\frac{k_x}{\rho} + \frac{k_{0x}}{\rho_0} = 0 \tag{2.68}$$

In Eq. (2.68), it is found that negative mass $\rho < 0$ is the necessary condition of the surface resonant states. To proceed, the transmission coefficient of a flat slab for different k_y is expressed as

$$T(k_y) = \frac{4\rho_0 \rho k_{0x} k_x e^{ik_x h}}{(\rho_0 k_x + \rho k_{0x})^2 - (\rho_0 k_x - \rho k_{0x})^2 e^{2ik_x h}} \tag{2.69}$$

The surface state condition (2.67) exactly ensures the denominator of the transmission coefficient vanishing, so that evanescent waves can be efficiently coupled to the surface state and their amplitudes are resonantly enhanced. Notice that the coupling effect between the surface modes and evanescent waves will result in the non-uniform enhancement for evanescent waves of different spatial frequencies, therefore the created image may be distorted. The evanescent wave enhancement by negative-mass metamaterials has been validated by numerical simulation [59] and experiment [60].

Acoustic metamaterials with anisotropic mass provide an alternative approach to overcome the diffraction limit [61, 62]. Suppose a flat slab with a mass tensor $\tilde{\rho} = \mathrm{diag}[\rho_\perp, \rho_\parallel]$, the dispersion relation is written as [63]

$$\frac{k_x^2}{\rho_\perp} + \frac{k_y^2}{\rho_\parallel} = \frac{\omega^2}{\kappa} \tag{2.70}$$

where k_x and k_y are respectively the wave vectors perpendicular and parallel to the slab surface. When $\rho_\parallel \rightarrow \infty$, and $\rho_\perp$ is around the mass density of the background material, evanescent waves could be converted to propagating waves with the same wave vector $k_x = \omega\sqrt{\rho_\perp/\kappa}$. In this case, all evanescent wave components will be transferred to the output side of the slab lens to form super-resolution images. In practice, the infinite mass can be realized in steel or brass slabs by the extremely large impedance mismatch between the metal slab and surrounding air [64, 65]. For either propagating or evanescent waves incident on a flat slab of anisotropic mass, the general expressions of transmission coefficients are the same to Eq. (2.69), but with the dispersion relation (2.70) used for the slab material and $\rho = \rho_\perp$. For complete transmission of evanescent waves through the slabs, the Fabry–Pérot resonant condition $k_x h = n\pi (n = 1, 2, \ldots)$ should be satisfied [65, 66]. Experiments based on such mechanism have been performed by Zhu *et al.* [65] and the spatial resolution $\lambda/50$ of deep subwavelength is achieved. Since evanescent waves with different k_y are transmitted with the unity modulus, the created image will not be distorted.

There is the other possibility coming from the impedance matching condition $\rho_0/k_{0x} = \rho_\perp/k_x$ to efficiently transfer evanescent waves, from Eq. (2.69) it is obtained that [67]

$$\left(1 - \frac{\rho_0^2}{\rho_\perp \rho_\parallel}\right) k_y^2 = \omega^2 \rho_0^2 \left(\frac{1}{\rho_0 \kappa_0} - \frac{1}{\rho_\perp \kappa}\right) \tag{2.71}$$

If the impedances are matched for arbitrary k_y, the following two relations should be satisfied

$$\rho_0^2 = \rho_\perp \rho_\parallel \quad \rho_0 \kappa_0 = \rho_\perp \kappa \tag{2.72}$$

Since $\rho_\parallel = \infty$ is necessary, Eq. (2.72) suggests $\rho_\perp \rightarrow 0$. Taking the limit $\rho_\perp \rightarrow 0$ and $\rho_\parallel \rightarrow \infty$ in Eq. (2.69), the transmission coefficient becomes

$$t = \frac{1}{1 - \frac{i\pi h/(\alpha\lambda_0)}{\sqrt{1 - k_y^2/k_0^2}}} \tag{2.73}$$

where $\alpha = \kappa/\kappa_0$ and λ_0 is the wavelength in the background material. In order for the high transmission of evanescent waves, it is necessary that $h/(\alpha\lambda_0) << 1$. One possibility for this condition

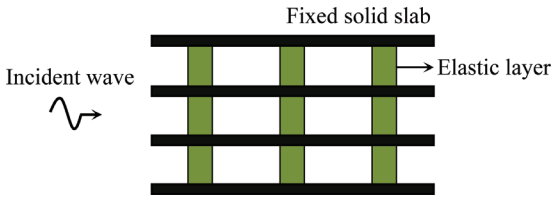

Figure 2.18 The model of a metamaterial superlens.

being satisfied is to increase α, and when α is sufficiently large, the second requirement in Eq. (2.72) for the impedance matching will be fulfilled, leading to the total transmission. The other choice is to decrease the relative thickness h/λ_0 of the slab. This process aims to make the lens as acoustically thin as possible and high transmission can be explained by the mass law, which states that the transmittance is inversely proportional to the material thickness. It is then demonstrated that a slab material of anisotropic mass $\rho_\perp \to 0$ and $\rho_\parallel \to \infty$ can enable efficient transmission of both propagating and evanescent waves as long as the condition $h/(\alpha\lambda_0) << 1$ is satisfied. The operating frequency of such lens will depend on the way how zero effective mass is realized. Based on the metamaterial technology, a lens with zero effective mass has been designed with the operating frequency invariant to the material thickness [67], in contrast to the lens based on the Fabry–Pérot resonance [65].

The designed lens consists of solid slabs with a periodic array of slits partially filled by elastic layers, as shown in Fig. 2.18. When the microstructure sizes are much less than the operating wavelength, the dynamic property of the slab lens can be well characterized by effective medium theory. The solid slabs are all fixed, so that infinite effective mass of the lens in the vertical direction is strictly satisfied. In the horizontal direction, the clamped elastic layers inside the slits undergo resonances at their lowest eigenfrequency. It has been shown in Section 2.2.1 that the resonant vibration of clamped layers will result in effective mass following the Drude-form expression $\rho_\perp = \rho(1 - \omega_0^2/\omega^2)$. Zero effective mass can be realized at the cutoff frequency ω_0. To verify the imaging effect, two monopole line sources separated by around $\lambda_0/9$ are placed in front of the designed lens and the image plane is taken closely behind the lens. Figure 2.19

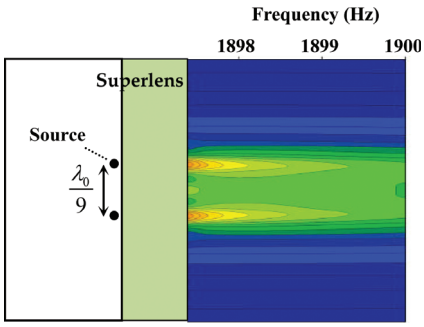

Figure 2.19 Contour plot of pressure amplitude distributions in the image plane taken closely behind the slab lens around the designed frequency 1898 Hz for two monopole line sources separated by about one ninth of the wavelength and placed in front of the lens.

shows the contour plots of pressure amplitude distributions in the image plane around the designed frequency 1898 Hz. It can be seen that the distance between two sources, which is less than the half wavelength, can be clearly distinguished from the images. These results demonstrate that the metamaterial superlens can create the images with spatial resolution beyond the diffraction limit.

2.5 Conclusions

In this chapter, we have introduced the fundamental properties of elastic metamaterials and several topics selected among their applications. We have shown the underlying mechanism how wave interactions with elastic metamaterials lead to negative values of effective dynamic mass, bulk or shear modulus. The understanding on these mechanisms will be helpful in developing different types of elastic metamaterials. Salient characteristics of metamaterials are demonstrated through different examples. Cloaking and superlensing effects of metamaterials are introduced as two examples of their interesting applications, and the principle and design methods are explained in details. It is expected that many more applications will be discovered in the near future.

References

1. Veselago, V. G. (1968). The electrodynamics of substances with simultaneously negative values of [permittivity] and [permeability], *Sov. Phys. Usp.,* **10**, pp. 509–514.
2. Pendry, J. B., Holden, A. J., Stewart, W. J., and Youngs, I. I. (1996). Extremely low frequency plasmons in metallic mesostructures, *Phys. Rev. Lett.,* **76**, pp. 4773–4776.
3. Pendry, J. B., Holden, A. J., Robbins, D. J., and Stewart, W. J. (1999). Magnetism from conductors and enhanced nonlinear phenomena, *IEEE Trans. Microwave Theory Tech.,* **47**, pp. 2075–2084.
4. Smith, D. R., and Kroll, N. (2000). Negative refractive index in left-handed materials, *Phys. Rev. Lett.,* **85**, pp. 2933–2936.
5. Smith, D. R., Padilla, W. J., Vier, D. C., Nemat-Nasser, S. C., and Schultz, S. (2000). Composite medium with simultaneously negative permeability and permittivity, *Phys. Rev. Lett.,* **84**, pp. 4184–4187.
6. Smith, D. R., Pendry, J. B., and Wiltshire, M. C. (2004). Metamaterials and negative refractive index, *Science,* **305**, pp. 788–792.
7. Lamb, H. (1904). On group-velocity, *Proc. London Math. Soc.,* **1**, pp. 473–479.
8. Pocklington, H. C. (1905). Growth of a wave-group when the grou-velocity is negative, *Nature,* **71**, pp. 607–608.
9. Liu, Z., Zhang, X., Mao, Y., Zhu, Y. Y., Yang, Z., Chan, C. T., and Sheng, P. (2000). Locally resonant sonic materials, *Science,* **289**, pp. 1734–1736.
10. Fang, N., Xi, D., Xu, J., Ambati, M., Srituravanich, W., Sun, C., and Zhang, X. (2006). Ultrasonic metamaterials with negative modulus, *Nat. Mater.,* **5** pp. 452–456.
11. Ding, Y., Liu, Z., Qiu, C., and Shi, J. (2007). Metamaterial with simultaneously negative bulk modulus and mass density, *Phys. Rev. Lett.,* **99**, pp. 093904.
12. Liu, X. N., Hu, G. K., Huang, G. L., and Sun, C. T. (2011). An elastic metamaterial with simultaneously negative mass density and bulk modulus, *Appl. Phys. Lett.,* **98**, pp. 251907.
13. Zhou, X., and Hu, G. (2009). Analytic model of elastic metamaterials with local resonances, *Phys. Rev. B,* **79**, pp. 195109.
14. Lai, Y., Wu, Y., Sheng, P., and Zhang, Z. Q. (2011). Hybrid elastic solids, *Nat. Mater.,* **10**, pp. 620–624.

15. Lee, S. H., Park, C. M., Seo, Y. M., Wang, Z. G., and Kim, C. K. (2009). Acoustic metamaterial with negative density, *Phys. Lett. A,* **373**, pp. 4464–4469.
16. Yao, S., Zhou, X., and Hu, G. (2010). Investigation of the negative-mass behaviors occurring below a cut-off frequency, *New J. Phys.,* **12**, pp. 103025.
17. Chan, C. T., Li, J., and Fung, K. H. (2006). On extending the concept of double negativity to acoustic waves, *J. Zhejiang Univ. Sci. A,* **7**, pp. 24–28.
18. Milton, G. W., and Willis, J. R. (2007). On modifications of Newton's second law and linear continuum elastodynamics, *Proc. R. Soc. London Ser. A,* **463**, pp. 855–880.
19. Yao, S., Zhou, X., and Hu, G. (2008). Experimental study on negative effective mass in a 1D mass–spring system, *New J. Phys.,* **10**, pp. 043020.
20. Huang, H. H., and Sun, C. T. (2009). Wave attenuation mechanism in an acoustic metamaterial with negative effective mass density, *New J. Phys.,* **11**, pp. 013003.
21. Baz, A. (2009). The structure of an active acoustic metamaterial with tunable effective density, *New J. Phys.,* **11**, pp. 123010.
22. Airoldi, L., and Ruzzene, M. (2011). Design of tunable acoustic metamaterials through periodic arrays of resonant shunted piezos, *New J. Phys.,* **13**, pp. 113010.
23. Chen, H., and Chan, C. T. (2007). Acoustic cloaking in three dimensions using acoustic metamaterials, *Appl. Phys. Lett.,* **91**, pp. 183518.
24. Hu, J., Zhou, X., and Hu, G. (2009). A numerical method for designing acoustic cloak with arbitrary shapes, *Comp. Mat. Sci.,* **46**, pp. 708–712.
25. Cummer, S. A., and Schurig, D. (2007). One path to acoustic cloaking, *New J. Phys.,* **9**, pp. 45.
26. Cummer, S., Popa, B.-I., Schurig, D., Smith, D., Pendry, J., Rahm, M., and Starr, A. (2008). Scattering theory derivation of a 3D acoustic cloaking shell, *Phys. Rev. Lett.,* **100**, pp. 024301.
27. Milton, G. W., Briane, M., and Willis, J. R. (2006). On cloaking for elasticity and physical equations with a transformation invariant form, *New J. Phys.,* **8**, pp. 248–248.
28. Hu, J., Chang, Z., and Hu, G. (2011). Approximate method for controlling solid elastic waves by transformation media, *Phys. Rev. B,* **84**, pp. 201101.
29. Chang, Z., Hu, J., Hu, G., Tao, R., and Wang, Y. (2011). Controlling elastic waves with isotropic materials, *Appl. Phys. Lett.,* **98**, pp. 121904.

30. Yang, Z., Mei, J., Yang, M., Chan, N., and Sheng, P. (2008). Membrane-type acoustic metamaterial with negative dynamic mass, *Phys. Rev. Lett.,* **101**, pp. 204301.
31. Lakes, R. S., Lee, T., Bersie, A., and Wang, Y. C. (2001). Extreme damping in composite materials with negative-stiffness inclusions, *Nature,* **410**, pp. 565–567.
32. Yao, S., Zhou, X., and Hu, G. (2008). Experimental study on negative effective mass in a 1D mass–spring system, *Proc. XXII ICTAM,* Adelaide, Australia.
33. Huang, H. H., and Sun, C. T. (2010). Theoretical investigation of the behavior of an acoustic metamaterial with extreme Young's modulus, *J. Mech. Phys. Solids,* **59**, pp. 2070–2081.
34. Liu, X. N., Hu, G. K., Sun, C. T., and Huang, G. L. (2011). Wave propagation characterization and design of two-dimensional elastic chiral metacomposite, *J. Sound Vib.,* **330**, pp. 2536–2553.
35. Wu, Y., and Zhang, Z. Q. (2009). Dispersion relations and their symmetry properties of electromagnetic and elastic metamaterials in two dimensions, *Phys. Rev. B,* **79**, pp. 195111.
36. Li, J., and Chan, C. (2004). Double-negative acoustic metamaterial, *Phys. Rev. E,* **70**, pp. 055602.
37. Alù, A., and Engheta, N. (2005). Achieving transparency with plasmonic and metamaterial coatings, *Phys. Rev. E,* **72**, pp. 016623.
38. Zhou, X., and Hu, G. (2006). Design for electromagnetic wave transparency with metamaterials, *Phys. Rev. E,* **74**, pp. 026607.
39. Zhou, X., and Hu, G. (2007). Acoustic wave transparency for a multilayered sphere with acoustic metamaterials, *Phys. Rev. E,* **75**, pp. 046606.
40. Zhou, X., Hu, G., and Lu, T. (2008). Elastic wave transparency of a solid sphere coated with metamaterials, *Phys. Rev. B,* **77**, pp. 024101.
41. Leonhardt, U. (2006). Optical conformal mapping, *Science,* **312**, pp. 1777–1780.
42. Pendry, J. B., Schurig, D., and Smith, D. R. (2006). Controlling electromagnetic fields, *Science,* **312**, pp. 1780–1782.
43. Greenleaf, A., Kurylev, Y., Lassas, M., and Uhlmann, G. (2007). Full-Wave invisibility of active devices at all frequencies, *Commun. Math. Phys.,* **275**, pp. 749–789.
44. Milton, G. W. (2002) *The theory of composites*. (Cambridge University Press, Cambridge).

45. Guild, M. D., Alu, A., and Haberman, M. R. (2011). Cancellation of acoustic scattering from an elastic sphere, *J. Acoust. Soc. Am.,* **129**, pp. 1355.
46. Norris, A. N. (2008). Acoustic cloaking theory, *Proc. R. Soc. London Ser. A,* **464**, pp. 2411–2434.
47. Zhang, S., Xia, C., and Fang, N. (2011). Broadband acoustic cloak for ultrasound waves, *Phys. Rev. Lett.,* **106**, pp. 024301.
48. Hu, J., Zhou, X., and Hu, G. (2009). Design method for electromagnetic cloak with arbitrary shapes based on Laplace's equation, *Opt. Express,* **17**, pp. 1308–1320.
49. Hu, J., Zhou, X., and Hu, G. (2009). Nonsingular two dimensional cloak of arbitrary shape, *Appl. Phys. Lett.,* **95**, pp. 011107.
50. Chang, Z., Zhou, X., Hu, J., and Hu, G. (2010). Design method for quasi-isotropic transformation materials based on inverse Laplace's equation with sliding boundaries, *Opt. Express,* **18**, pp. 6089–6096.
51. Popa, B.-I., and Cummer, S. A. (2011). Homogeneous and compact acoustic ground cloaks, *Phys. Rev. B,* **83**, pp. 224304.
52. Popa, B.-I., Zigoneanu, L., and Cummer, S. A. (2011). Experimental acoustic ground cloak in air, *Phys. Rev. Lett.,* **106**, pp. 253901.
53. Brun, M., Guenneau, S., and Movchan, A. B. (2009). Achieving control of in-plane elastic waves, *Appl. Phys. Lett.,* **94**, pp. 061903.
54. Chang, Z., Hu, J., and Hu, G. K. (2010). Transformation method and wave control, *Acta Mech. Sin.,* **26**, pp. 889–898.
55. Zhang, X., and Liu, Z. (2008). Superlenses to overcome the diffraction limit, *Nat. Mater.,* **7**, pp. 435–441.
56. Pendry, J. B. (2000). Negative refraction makes a perfect lens, *Phys. Rev. Lett.,* **85**, pp. 3966–3969.
57. Zhang, S., Yin, L., and Fang, N. (2009). Focusing ultrasound with an acoustic metamaterial network, *Phys. Rev. Lett.,* **102**, pp. 194301.
58. Ambati, M., Fang, N., Sun, C., and Zhang, X. (2007). Surface resonant states and superlensing in acoustic metamaterials, *Phys. Rev. B,* **75**, pp. 195447.
59. Deng, K., Ding, Y., He, Z., Zhao, H., Shi, J., and Liu, Z. (2009). Theoretical study of subwavelength imaging by acoustic metamaterial slabs, *J. Appl. Phys.,* **105**, pp. 124909.
60. Park, C., Park, J., Lee, S., Seo, Y., Kim, C., and Lee, S. (2011). Amplification of acoustic evanescent waves using metamaterial slabs, *Phys. Rev. Lett.,* **107**, pp. 194301.

61. Ao, X., and Chan, C. T. (2008). Far-field image magnification for acoustic waves using anisotropic acoustic metamaterials, *Phys. Rev. E,* **77**, pp. 025601.
62. Li, J., Fok, L., Yin, X., Bartal, G., and Zhang, X. (2009). Experimental demonstration of an acoustic magnifying hyperlens, *Nat. Mater.,* **8**, pp. 931–934.
63. Torrent, D., and Sánchez-Dehesa, J. (2010). Anisotropic mass density by radially periodic fluid structures, *Phys. Rev. Lett.,* **105**, pp. 174301.
64. Jia, H., Ke, M., Hao, R., Ye, Y., Liu, F., and Liu, Z. (2010). Subwavelength imaging by a simple planar acoustic superlens, *Appl. Phys. Lett.,* **97**, pp. 173507.
65. Zhu, J. (2010). A holey-structured metamaterial for acoustic deep-subwavelength imaging, *Nat. Phys.,* **7**, pp. 52–55.
66. Liu, F., Cai, F., Peng, S., Hao, R., Ke, M., and Liu, Z. (2009). Parallel acoustic near-field microscope: A steel slab with a periodic array of slits, *Phys. Rev. E,* **80**, pp. 026603.
67. Zhou, X., and Hu, G. (2011). Superlensing effect of an anisotropic metamaterial slab with near-zero dynamic mass, *Appl. Phys. Lett.,* **98**, pp. 263510.